Acta Astronautica 188 (2021) 438–450

Contents lists available at ScienceDirect

Acta Astronautica

journal homepage: www.elsevier.com/locate/actaastro

Research paper

Hypothetical Apophis deep ocean impact—Energy analysis

Renato H. Morais [a], Luís F.F.M. Santos [a,b,*], André R.R. Silva [a], Rui Melicio [c,d]

[a] LAETA-AEROG, Universidade da Beira Interior, Covilhã, Portugal
[b] ISEC Lisboa, Portugal
[c] LAETA-IDMEC, Instituto Superior Técnico, Universidade de Lisboa, Portugal
[d] ICT, Escola de Ciências e Tecnologia, Universidade de Évora, Évora, Portugal

ARTICLE INFO

Keywords:
NEO
Apophis
Asteroid impact
Impact effects
Short-term consequences
Vulnerabilities

ABSTRACT

This paper models a hypothetical Apophis asteroid impact on an chosen deep ocean point on the globe. To assess the potential vulnerabilities of an exposed coast population, the impact effects were assessed as a function of the distance to the asteroid's impact point as well as altitude for the tsunami case. All the tools and models used are valid and can be implemented for any other point on the Earth's surface. The impact modelling includes the analysis of cratering formation, generated earthquake, overpressure, ejected material, generated thermal radiation and tsunami, as well as the global geophysical effects of the impact. The vulnerability models entail best, expected, and worst case scenarios, which allows a reasonable range of results. As the impact occurs in the ocean, and if its a great distance away from populated areas, the population is safeguarded from most of the impact effects. The tsunami is undoubtedly the most far-reaching and threatening impact effect from an asteroid impact on the ocean.

1. Introduction

When analysing Earth astronomical impacts, we need to tell the story of Earth creation. Earth creation is tightly connected to asteroid impacts, as it has been the target of several collision events throughout its history. The most notorious event is the one theorized to have generated the Chicxulub crater in Mexico and marked the ending of the Cretaceous period [1,2]. However, this is not some distant past threat. In 2013 the airburst of a small body roughly 20 m wide, which became known as the Chelyabinsk meteor, injured about 1500 people and damaged thousands of buildings [3]. A single individual is unlikely to experience the impact of a major Near-Earth Object (NEO) during their lifetime, however, the potential consequences of an impact event can be extreme. The impact hazard has similarities with familiar natural destructive processes, such as earthquakes, fires, falling debris, and floods, with the added harm of not being location-dependent [4].

The Apophis asteroid was discovered in 2004 and has an estimated diameter of 370 m [5,6]. It is one of the most notorious asteroids due to a non-trivial probability of impact in 2029, given initial observations. This claim was dismissed with updated observations, however, a future impact in 2036 remained a possibility [7]. The Apophis asteroid reached an unprecedented value of 4 on the Torino scale. Newer observations denied the 2036 impact possibility [8], and the Apophis has been reassigned the value 0. However, collision remained a possibility from 2060 onwards, reaffirming the importance of studying the Apophis asteroid orbit and physical properties [9,10]. As of March 2021, a 2068 impact as been confidently ruled out, as well as the impact risk in the next one hundred years, being removed from NASA's Sentry Risk Table and disregarded as a hazardous object [11]. Based on the orbit [12] and the spectral type [13,14], the Apophis is an Aten asteroid and an Sq-type asteroid, respectively. Observations made state the resemblance between the Apophis and an LL ordinary chondrite meteorite which allowed the estimation of its bulk density to 3.2 g/cm^3 [15].

In [16] are presented celestial objects that pose the greatest risk to populations and infrastructures. The majority of these are between 300 and 1000 m in diameter. The impact of these objects is more frequent than larger ones and can still produce impact events on a global scale. Different types of missions capable of altering the orbit of hazardous asteroids to mitigate the risk, like kinetic impactors [17], gravity tractors [18], nuclear detonation [19], and even ion beams produced by a shepherd aircraft [20], have been studied by the scientific community. Each method has a different level of effectiveness, however any mitigation measure can be adopted and be successful depending on the situation. Nonetheless, the aftermath of the deflection mission still needs to be considered, to ensure that the impact location is not moved to a point where it remains a threat to different populations [21]. The technology able to fend off such threats is currently available if we

* Corresponding author at: ISEC Lisboa, Portugal.
E-mail address: luis.santos@iseclisboa.pt (L.F.F.M. Santos).

https://doi.org/10.1016/j.actaastro.2021.08.005
Received 22 April 2021; Received in revised form 28 July 2021; Accepted 2 August 2021
Available online 8 August 2021

are given enough time to prepare, which gives great importance to the constant observations and discoveries of new potential hazardous asteroids.

Several authors already studied and modelled Earth impacts by external bodies. In [22] are developed algorithms to quantify the principal impact effects that might affect people, infrastructure, and landscapes in the area surrounding an impact event. These new algorithms include the estimation of the asteroid's atmospheric passage aftermath, the thermal radiation emitted, and the seismic shock intensity. It also includes estimations for the impact crater dimensions and ejecta deposits, as well as the severity of air blast from either airbursts or surface impacts.

In [23] are estimated the virtual impacts of the 315 asteroids on NASA's NEO risk list, which includes an assessment of the impact location probability distribution. In [24,25] are reassessed the impacts corridors for 261 observed asteroids that could impact the Earth before the year 2100. The impact probability distributions were projected onto a world map. The cumulative impact probability distribution coupled with the Earth population produces a risk map that identifies which nations are more susceptible to an asteroid impact.

In [26] is developed a tool to evaluate the impact risks of menacing asteroids. The developed method expresses the risk in terms of expected casualties and allows the comparison with other natural disasters. To assess the risk, the author extrapolated and exposed vulnerability models that, given the severity of an impact effect, allow the estimation of the affected population and enable the establishment of the most dangerous impact effects.

A water impact differs from a land impact in several aspects. Oceans cover approximately 70% of Earth's surface, making future and past ocean impacts more probable. To quantify the hazard posed by future ocean impacts, the impact of a celestial body in the ocean and the generation of large tsunami waves was studied. A water depth of 6–8 times the diameter of a stony asteroid was claimed to be sufficient to completely suppress the benthic cratering formation. In an ocean impact there is the formation of two different types of tsunami waves: rim waves and collapse waves, both with little in common with traditional earthquake induced tsunami waves [27].

2. Modelling

The authors follow a symbolic-numerical calculation to obtain the data for each point of interest. The authors also put into consideration several premises to obtain more direct results. Is important to refer that the impact is guaranteed, and no additional orbital mechanics calculations are required. It is also considered that the population is not warned about the impact, since it is impossible to obtain the population vulnerability if otherwise. Only the direct effects are considered, so atmospheric and terrain reflections are disregarded.

The impact effects and vulnerability assessment is highly dependent on the distance to the impact site, as such, the great-circle distance between the impact site and the point of interest is given by:

$$D = R_E \arccos\left[\sin\phi_i \sin\phi_k + \cos\phi_i \cos\phi_k \cos\left(|\lambda_i - \lambda_k|\right)\right] \tag{1}$$

where D is the distance to the impact site, R_E is the Earth's radius, ϕ and λ are respectively latitude and longitude, and finally coefficients i and k represent the impact location and point of interest respectively.[1]

The asteroid destructive potential is directly related to the impact energy, which is related to the impact angle and speed. Since this analysis assumes an oceanic impact, there are two moments of interest, the first is the impact with the ocean surface, at sea level. The second with the ocean floor. In [22], a simple relation was provided that allows the estimation of the water layer effects on the asteroid's velocity. The equation computes the impactor's velocity at the seafloor, $v_{i_{seafloor}}$, as a function of the impactor's velocity at the surface, $v_{i_{surface}}$, as:

$$v_{i_{seafloor}} = v_{i_{surface}} e^{\frac{3\rho_w C_D h_{sea}}{2\rho_i L \sin\theta}} \tag{2}$$

In the previous equation, ρ_w and ρ_i are the water and impactor densities, h_{sea} is the ocean floor's depth, L is the asteroid's diameter, θ is the impact angle and C_D is the drag coefficient for a rigid sphere in the supersonic regime, which was set to 0.887 by the author.

Both the impact energy at the surface $E_{surface}$ and the energy at the sea floor $E_{seafloor}$ can be acquired using the impact velocities $v_{i_{seafloor}}$ and $v_{i_{surface}}$, respectively. The air blast and thermal radiation models assume that the impact energy that catalyses these effects is released at the surface. On the other hand, effects such as seismic shaking and ejecta deposition occur on solid target impacts, thus the impact energy is assumed to be the ocean floor kinetic energy. These assumptions imply that a land and water impact of the same impact energy are equivalent in terms of the air blast and thermal radiation generated. However, the water column presence could attenuate the seismic shaking intensity and the ejecta released when compared to a ground impact scenario.

2.1. Cratering

The complexity of the cratering process hinders the crater dimensions modelling. The process can be broken down into two stages, the formation of a transient crater and the formation of the final crater. The transient crater is an unstable structure that cannot support itself, it eventually collapses and forms the final crater. In [22] and later in [26] analytical relations to express the crater dimension were presented, which were developed through the use of scaling laws and empirical data. The following equation expresses the transient crater diameter D_{tc}, in metres, as a function of the initial parameters of the impact: the density of the target ρ_t and impactor ρ_i, the impactor's diameter L, the impact velocity v_i, the angle of impact θ, and the Earth's standard gravitational acceleration g_0:

$$D_{tc} = 1.161 \left(\frac{\rho_i}{\rho_t}\right)^{1/3} L^{0.78} v_i^{0.44} g_0^{-0.22} \sin^{1/3}\theta \tag{3}$$

For impacts on liquid surfaces, the scalar 1.161 must be changed to 1.365 in (3). In terms of crater diameter, the threshold between simple and complex craters is 3.2 km. For simple craters, the final crater diameter, from rim-to-rim, is:

$$D_{fr} = 1.25 D_{tc} \tag{4}$$

if the transient crater is greater than 2.56 km, the final crater diameter can be expressed as:

$$D_{fr} = 1.17 \frac{D_{tc}^{1.13}}{D_c^{0.13}} \tag{5}$$

where D_c is the 3.2 km threshold diameter. To assess the depth for the transient crater in relation to the original ground plane the following relation can be used:

$$d_{tc} = \frac{D_{tc}}{2\sqrt{2}} \tag{6}$$

The complex final crater depth, in km, is defined in [28] as:

$$d_{fr} = 0.294512 D_{tc}^{0.34013} \tag{7}$$

for the simple final crater, the depth is simply given by:

$$d_{fr} = d_{tc} + h_{fr} - t_{br} \tag{8}$$

where h_{fr} and t_{br} are the rim height and the thickness of the Breccia lens, respectively. Both parameters are given by the following

[1] See Nomenclature at end of paper.

expressions (9) and (10):

$$h_{fr} = 0.03584 D_{tc} \tag{9}$$

$$t_{br} = 0.123354 D_{tc} \tag{10}$$

The unbulked Breccia lens volume V_{br} is assumed to be related to the final crater diameter by:

$$V_{br} = 0.0625 D_{tc}^3 \tag{11}$$

Finally, the volume of the transient crater can be expressed as:

$$V_{tc} = 0.13884 D_{tc}^3 \tag{12}$$

2.2. Seismic shock

Given a solid surface impact event, a seismic shock is generated that is intrinsically related to the impactor's kinetic energy. The Gutenberg–Ritcher magnitude energy relation, referenced in [22] and later in [26], gives us the absolute seismic magnitude at the impact location as a function of its kinetic energy:

$$M = 0.67 \log_{10} E - 5.87 \tag{13}$$

where E is the kinetic energy in Joules and M the magnitude on the Ritcher scale. The seismic intensity experienced decays over the travelled distance. The effective magnitude M_{eff} felt on a specific location, at a distance D from the impact point, was expressed in [22] and later in [26] by the following relation:

$$M_{eff} = \begin{cases} M - 2.38 \times 10^{-5} D & : 1 \\ M - 4.8 \times 10^{-6} D - 1.1644 & : 2 \\ M - 1.66 \log_{10} \Delta - 6.399 & : 3 \end{cases} \tag{14}$$

where Δ is the epicentral angle in radians between the impact point and relevant location defined in (21). In (14), case 1 is valid for D values less than 60 km, case 2 is valid when D ranges from 60 km to 700 km, and case 3 is valid for D values equal or greater than 700 km.

2.3. Air blast

Similar to explosions, a very known field of study, asteroid impact events create air blasts, shock waves that increase the atmospheric pressure at the wavefront. Relying on yield scaling, the distance D_1 can be found. The yield scaled distance D_1 experiences the same peak overpressure from a 1 kt energy impact as the distance D experiences from an E_{kt} energy impact and can be given by:

$$D_1 = \frac{D}{E_{kt}^{1/3}} \tag{15}$$

where D is the distance in metres from the impact location and E_{kt} is the energy in kilotons TNT. The peak overpressure decay in Pa as a function of the yield scaled distance D_1 can be obtained by:

$$p_D = \frac{p_x D_x}{4 D_1} \left(1 + 3 \left[\frac{D_x}{D_1} \right]^{1.3} \right) \tag{16}$$

where the values p_x and D_x that in [22] were found to best fit the empirical data provided by the US nuclear explosion tests were 75 000 Pa and 290 m, respectively.

2.4. Thermal radiation

In the vicinity of an impact event, the temperature and pressure are drastically raised during an impact event. In [22] and later in [26] a way to compute the thermal energy generated from an impact event was presented. For impact velocities greater than 12 km/s, the shock pressure can melt the impactor and some target material; for velocities greater than 15 km/s, vaporization begins to occur. The vapour generated has very high pressure and temperatures that expand rapidly, this process is named fireball. This thermal radiation model neglects the effect of atmospheric conditions and the variation in atmospheric absorption with altitude. The empirical relation between the radius of the fireball R_f in metres and the impact energy E in Joules is expressed as:

$$R_f = 0.002 E^{1/3} \tag{17}$$

The thermal radiation is only a fraction of the impactor's kinetic energy upon impact. This fraction, the luminous efficiency η_{lum}, for asteroid impacts with Earth is presently between $10^{-4} - 10^{-2}$, a range found through limited experimental and numerical results reflected in [22]. The thermal energy per area unit is obtained by:

$$\phi = f \frac{\eta_{lum} E}{2\pi D^2} \tag{18}$$

where f is the fraction of visible fireball over the horizon at distance D, given by:

$$f = \frac{2}{\pi} \left(\cos^{-1} \frac{h_f}{R_f} - \frac{h_f}{R_f} \sin \left[\cos^{-1} \frac{h_f}{R_f} \right] \right) \tag{19}$$

In (19), h_f is the maximum fireball height below the horizon at a distance D, and it is defined as:

$$h_f = (1 - \cos \Delta) R_E \tag{20}$$

where Δ is the angle given by:

$$\Delta = \arccos \left[\sin \phi_i \sin \phi_k + \cos \phi_i \cos \phi_k \cos \left(|\lambda_i - \lambda_k| \right) \right] \tag{21}$$

If $h_f \geq R_f$ then the fireball is entirely below the horizon, which means that there is no direct thermal radiation reaching the location defined by (21). If such scenario becomes a reality, and not having into account atmospheric radiation deflection, the thermal radiation of locations below the horizon will be zero.

2.5. Ejected material

The ejection of material from the impact site is one of the consequences of a solid surface collision. This ejected material, named ejecta, can endanger populations by being hurled directly to civilized areas, by forming a blanket of dense particles that covers the surroundings, or by damaging infrastructures to the point of collapse by deposition, or by direct collision. In [22] analytical expressions were deduced to estimate the mean ejecta fragment diameter and the ejecta blanket thickness that were later exposed in [26]. The mean ejecta fragment diameter L_e, in metres, can be expressed, as a function of the final crater diameter D_{fr} and distance D, as:

$$L_e = 2400 \left(\frac{D_{fr}}{2000} \right)^{-1.62} \left(\frac{D_{fr}}{2D} \right)^{2.65} \tag{22}$$

The ejecta blanket thickness t_e as a function of the transient crater diameter D_{tc} and the distance D is defined by:

$$t_e = \frac{D_{tc}^4}{112 D^3} \tag{23}$$

2.6. Tsunami

Following an asteroid impact on a liquid surface, a circular wave pattern is generated, like a droplet impacting a liquid film. These waves can have a tremendous reach and hit inhabited coastal regions, causing devastation in its wake. This is named a tsunami, it is a complex process and a complex effect to model.

The tsunami assessment can be divided in two stages: the deep-water wave propagation, and the wave run-up estimation, near the coast. The wave amplitude attenuation models estimate the evolution of the maximum wave amplitude in deep-waters, assuming a constant ocean depth. In shallow waters, assumed to be waters less than 800 m deep, the model estimates the run-up wave on the coast, given the wave amplitude at the deep/shallow water threshold, and assumes the ocean floor has a constant positive slope.

2.6.1. Rim-wave

The initial asteroid impact on the ocean surface radially displaces the water to create the surface transient crater. This displacement is the origin of the wave perturbation that eventually develops into the first tsunami wave, the rim-wave. In [28] a rim-wave amplitude propagation model was developed. The model has an amplitude decay with the radial distance of $1/D$, consistent with oceanic impact simulations [27]. The rim-wave maximum amplitude was given by:

$$A_{rw}^{max} = \min\left(\frac{D_{tc}}{14.1}, h_{sea}\right) \tag{24}$$

The rim-wave amplitude A_{rw} at a distance D from the impact location was defined as:

$$A_{rw} = A_{rw}^{max}\left(\frac{3D_{tc}}{4D}\right) \tag{25}$$

2.6.2. Collapse-waves

The second type of wave is a consequence of the surface transient crater collapse. The surface transient crater gets filled by the adjacent ocean through centripetal inflow. The radial inflow creates a water peak at the centre of the now collapsing crater that will continue to oscillate radially in and out until all energy is dissipated. Each oscillation generates a collapse wave. The model being exposed only assumes the formation of a single collapse wave. In [28] a model was defined to predict the collapse wave amplitude decay over the distance. The maximum collapse wave amplitude was expressed as:

$$A_{cw}^{max} = 0.06\ min\left(\frac{D_{tc}}{2.828}, h_{sea}\right) \tag{26}$$

The collapse wave amplitude decay as a function of the distance D was given by:

$$A_{cw} = A_{cw}^{max}\left(\frac{5D_{tc}}{2D}\right)^{q} \tag{27}$$

where q is the attenuation factor, defined by:

$$q = 3e^{-0.8L/h_{sea}} \tag{28}$$

which is only valid for $L/h_{sea} < 0.5$

2.6.3. Run-up

The wave run-up U was defined as the maximum vertical extent of the wave, given the slope s of the coastal region. In [26] a simple analytical model was developed to estimate the run-up U, that uses the following expression for its assessment:

$$U = 2sA_{800}\left(\frac{A_{800}}{D_{tc}}\right)^{-0.5} \tag{29}$$

where A_{800} is the wave amplitude when it reaches shallow waters, defined as being water less than 800 m deep. The shore slope s was simply defined by the rise over run formula:

$$s = \frac{|h_{800} - h|}{D_{shore}} \tag{30}$$

where D_{shore} is the distance from the 800 m depth point to the location, h_{800} is per definition −800 m and h is the location's altitude. However, the run-up is in relation to the sea level. Thus, a local run-up U_l was computed in which the altitude of the location is considered:

$$U_l = U - h \tag{31}$$

Therefore, the local run-up U_l will be the tool with which the tsunami vulnerability will be assessed.

Table 1
Global implications of an impact event [22].

Ratio	Interval	Qualitative global change
M_i/M_E	$]-\infty; 0.001[$	No noticeable change in orbit.
	$]0.001; 0.01[$	Noticeable change in orbit.
	$]0.01; 0.1[$	Substantial change in orbit.
	$]0.1; +\infty[$	Totally changes orbit.
Γ_i/Γ_E	$]-\infty; 0.01[$	No noticeable change in rotation period and tilt of axis.
	$]0.01; 0.1[$	Noticeable change in rotation period and tilt of axis.
	$]0.1; 1.0[$	Substantial change in rotation period and tilt of axis.
	$]1.0; +\infty[$	Totally changes rotation period and tilt of axis.
V_{tc}/V_E	$]-\infty; 0.1[$	Earth is not strongly disturbed and loses negligible mass.
	$]0.1; 0.5[$	Earth is strongly disrupted but loses a little mass.
	$]0.5; +\infty[$	Earth is completely disrupted and loses all mass.

2.7. Global effects

In [22] a straightforward way is presented to assess the global effect of an impact event by computing the linear and angular momentum ratios between the Earth and the impactor, as well as the volume ratio of the transient crater diameter and the Earth's volume.

The linear momentum of the impactor M_i can be obtained by relating its mass m_i and its impact velocity v_i, by:

$$M_i = m_i v_i \tag{32}$$

Earth's linear momentum is obtained in a similar way, assuming its mass being $m_E = 5.83 \times 10^{24}$ kg and its mean orbital velocity being $v_E = 29780$ m/s. The angular momentum of the impactor is defined by:

$$\Gamma_i = m_i v_i R_E \cos\theta \tag{33}$$

while Earth's angular momentum was assumed to be $\Gamma_E = 5.86 \times 10^{33}$ kg m^3 s^{-1}. The Earth's volume was obtained assuming a 6371 km radius sphere. Depending on these three ratios, the qualitative global implications of the impact can be observed in Table 1.

In [28] is presented a way to assess the change in the length of a day caused by impacts on Earth. The variation of the Earth's rotation period ΔT_E can be obtained relating the asteroid's mass m_i, velocity v_i and impact angle θ with Earth's radius R_E, mass m_E and rotation period T_E, through the relation:

$$\Delta T_E = \frac{5}{4\pi R_E}\frac{m_i}{m_E}\cos\theta\ v_i T_E^2 \tag{34}$$

2.8. Vulnerability

The vulnerability models estimate the population ratio victimized by each impact effect. Vulnerability is closely related to the severity of the impact effects, which in turn are a function of the distance. The vulnerability values range from 0 to 1. A result of 0 means that no population if affected by the impact effect, while a vulnerability of 1 signifies that the entire population is lethally harmed. So, for example, a value of $V_\phi = 0.5$ for $D = 50$ km represents a 50% death ratio due to thermal radiation, 50 km away from the impact site.

The models do not consider the time of day the impact event occurs, nor that the population has an anticipated warning about the threat. These models also fail to consider the terrain orography, the meteorological conditions, and the wind's direction. The models are also independent of one another. Meaning that the total impact vulnerability of a location is not the sum of each impact effect vulnerability.

2.8.1. Seismic shaking

To correlate the seismic shaking intensity with the vulnerability rate, in [29] a literature review was conducted to collect relevant data and derived a seismic shaking vulnerability model. The data set was ample, allowing the establishment of a best and worst-case scenario, along with an expected case. The following equation relates the seismic

Table 2
Seismic shaking vulnerability coefficients [29].

	a	b
Best	−2.51	−9.59
Expected	−2.52	−8.69
Worst	−3.80	−7.60

Table 3
Overpressure vulnerability coefficients [29].

	$a \times 10^5$	$b \times 10^{-5}$
Best	−1.90	−5.43
Expected	−2.42	−4.40
Worst	−2.85	−3.53

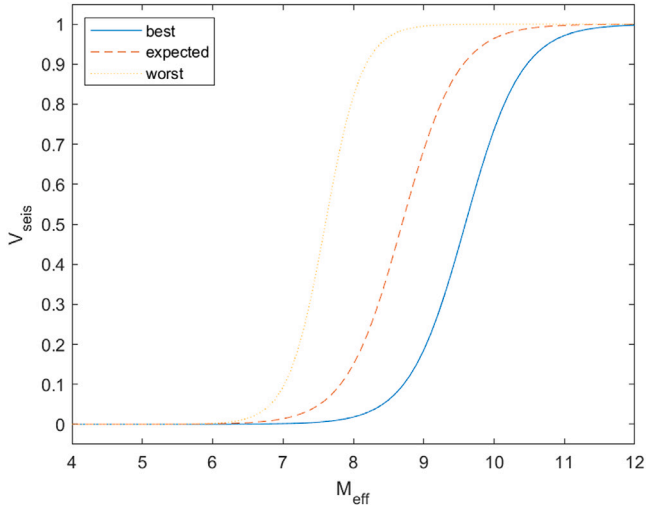

Fig. 1. Best, expected, and worst seismic shaking vulnerability models.

intensity on the Ritcher scale, on a given place, with the population vulnerability to that event. The equation representing the three cases are:

$$V_{\text{seis}} = \frac{1}{1 + e^{a(M_{eff}+b)}} \tag{35}$$

where a and b are coefficients derived from empirical data and validated against earthquake events [29] and presented in Table 2 for each one of the three cases, best, expected, and worst-case scenario. All three case-scenarios are represented graphically in Fig. 1.

2.8.2. Overpressure

Experiencing high pressure differentials can endanger the population. In [29] data regarding non-lethal, half lethal, and entirely lethal pressure differentials was used to extrapolate different case-scenario for the pressure vulnerability model. The model does not take into consideration the repercussions the pressure-damaged infrastructures have on the population. The vulnerability models as logistic functions are:

$$V_{\text{p}} = \frac{1}{1 + e^{a(p+b)}} \tag{36}$$

where the coefficients a and b are derived from experimental data and extrapolated form animal tests to humans [29]. The coefficients are presented in Table 3. In Fig. 2 the three vulnerability scenarios can be seen.

2.8.3. Thermal radiation

Thermal radiation can burn or ignite any surface it encounters. The skin is included as such surface, which makes thermal radiation potentially fatal to populations. To develop a thermal radiation vulnerability

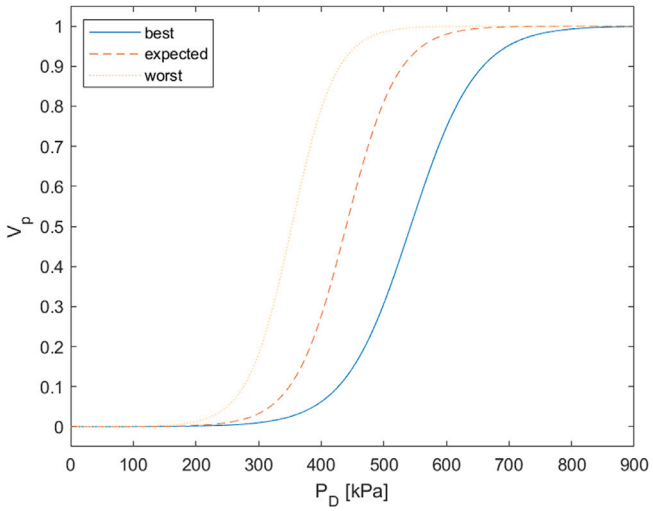

Fig. 2. Best, expected, and worst overpressure vulnerability models.

Table 4
Thermal radiation vulnerability coefficients [29].

	a	$b \times 10^6$	$c \times 10^{-5}$
Best	0.25	−5.62	−7.32
Expected	0.47	−5.62	−7.32
Worst	1.00	−5.62	−7.32

model, in [29] different types of data were gathered. It included the skin burn probability, the burn degree distribution as a function of the radiation exposure, and the mortality rate of treated and untreated burn victims as a function of burnt total body surface area. In the model development process, clothes were considered to offer a degree of protection and that only one person's side can be exposed to the radiation. Finally, to distinguish between different cases' vulnerability models, the author considered different percentages of sheltered population during the impact event. For the best-case scenario, all population is sheltered but 25% are affected via windows, for the expected case, the author assumed 47% of unsheltered population. In the worst-case scenario, all population is assumed to be unsheltered. The vulnerability model is given by:

$$V_{\phi} = \frac{a}{1 + e^{b(\phi+c)}} \tag{37}$$

The respective coefficient a represents the estimated percentage of exposed population, while b and c were derived from data relating radiant exposure with mortality rate [29]. All coefficients are presented in Table 4. All three thermal exposure vulnerability models are shown in Fig. 3.

2.8.4. Ejecta blanket deposition

The ejected material from the crater formation is a hazard to populations because its deposition on building can cause them to collapse due to the ejecta blanket weight load. The ejecta can also pose a threat by bludgeoning individuals. However, only the former peril was included in the vulnerability model. In [26] a model was developed that determines the vulnerability by a particular ejecta blanket thickness t_e. The authors assumed a mean ejecta material density ρ_e of 1600 kg m^{-3} to assess the load of the ejecta blanket, defined by:

$$p_e = t_e \rho_e g_0 \tag{38}$$

Rumpf et al. assumed that 78% of the affected population are indoors during an impact event. Given a collapse, Rumpf et al. also assumes that 20% of occupants of a given house would be trapped inside and that 50% of those would be fatalities. Thus, in a roof collapse event,

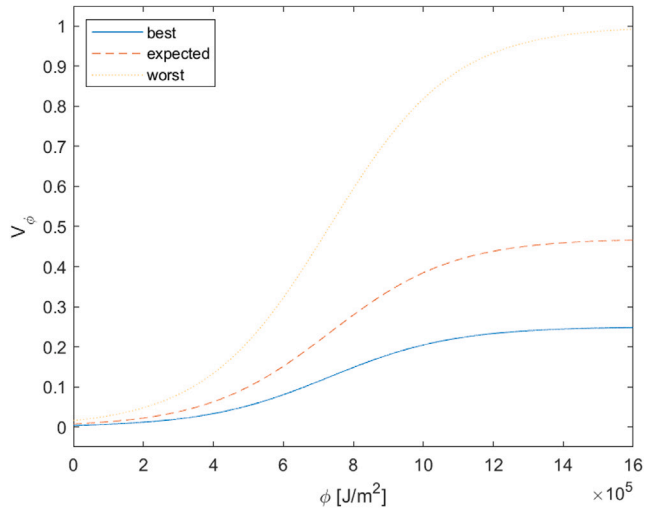

Fig. 3. Best, expected, and worst thermal radiation vulnerability models.

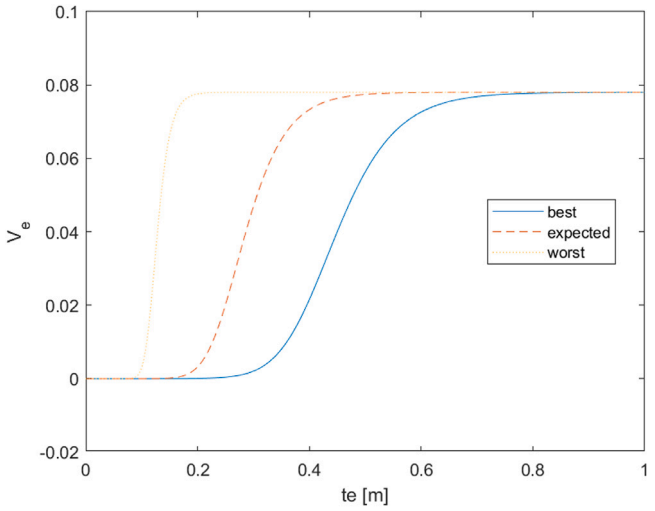

Fig. 4. Best, expected, and worst ejecta blanket deposition vulnerability models.

the maximum population vulnerability is $0.78 \times 0.2 \times 0.5 = 0.078$. Best, expected, and worst-case scenarios were derived from different building strengths. The best-case scenario assumes the buildings have a strong frame, the worst-case scenario assumes the buildings are fragile in nature and the expected case scenario is a compromise between both. Therefore, the following ejecta vulnerability model computes the likelihood of a roof collapse due to the ejected material and the percentage of affected population if it collapses:

$$V_e = \frac{0.078}{\left[1 + e^{a(p_e+b)}\right]^c} \tag{39}$$

where the ejecta load p_e is in kPa. In turn, the coefficients a, b, and c vary depending on the case scenario, are derived from collected data on building strength and roof types [29], and are presented in Table 5. Fig. 4 represents all three vulnerability cases.

2.8.5. Tsunami

A large wave can be devastating when hitting a coastal region. Estimating the consequences of a tsunami is no easy task due to is its high complexity. A simple analytical approach to assess the behaviour of the tsunami wave and its subsequent fatalities was developed in [29].

Table 5
Ejecta blanket deposition vulnerability coefficients [29].

	a	b	c
Best	−1.00	−5.84	−2.58
Expected	−1.37	−3.14	−4.60
Worst	−4.32	−1.61	−4.13

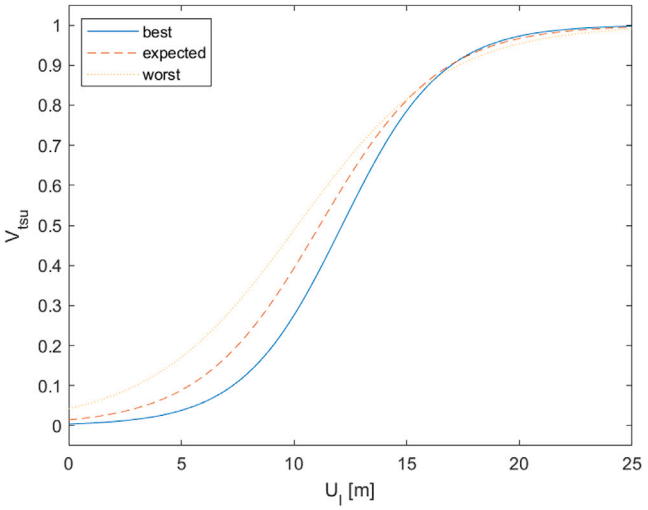

Fig. 5. Best, expected, and worst tsunami vulnerability models.

Table 6
Tsunami vulnerability coefficients [29].

	$a \times 10^1$	$b \times 10^{-1}$	D_{shore} [km]
Best	−4.53	−1.21	100
Expected	−3.80	−1.11	10
Worst	−3.07	−1.02	1

A simple vulnerability computation is presented here that is a function of the local run-up wave U_l of each municipality. For each case scenario the local run-up was defined with different D_{shore} values. The vulnerability relation used was given by:

$$V_{tsu} = \frac{1}{1 + e^{a(U_l+b)}} \tag{40}$$

its coefficients, along with the D_{shore} values considered, are presented in Table 6 while the visual representation can be seen in Fig. 5. The coefficients resulted from a sigmoid function interpolation with the data provided [29].

3. Results and discussion

The case study assumes the hypothetical impact of the Apophis asteroid at a latitude of 39.6177°N and longitude of 16.9532°W, the chosen point lies between mainland Portugal, Madeira, and Azores, in the Atlantic Ocean, where the water is 4910 m deep. The location was chosen to allow the authors follow-up studies of the consequences of such impacts to the population. This study aims to assess the impact effects attenuation and its vulnerabilities as a function of the distance to the impact site.

Apophis – measuring 370 m in diameter and weighing 3200 kg/m^3 – reaches the ocean with an impact velocity v_i of 12 620 m/s at a 45° angle θ, resulting in 6.8×10^{18} J of kinetic energy. The bottom of the ocean, 4910 metres deep, is reached at 5.630 m/s totalling an impact energy of 1.345×10^{12} J.

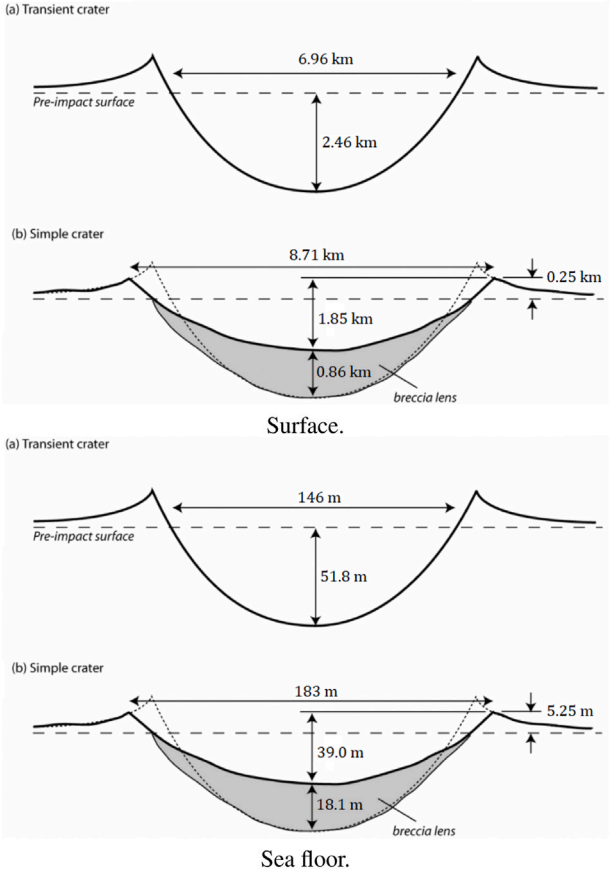

Fig. 6. Crater dimensions for the transient crater (a) and simple final crater (b), for the surface and sea floor cratering process.

3.1. Local impact effects

The crater dimensions, for the surface impact and the sea floor impact, were obtained via (3) through (12). Both final craters are simple. The theoretical visual representation of the final and transient craters can be seen in Fig. 6. The water surface transient crater spans, rim to rim, a little under 7 km. Therefore, the impact effects and vulnerability assessment only truly begins for $D > D_{tc}/2$. Any distance under the transient crater radius are within the crater formation zone and the vulnerability is assumed one. Any further impact effects and vulnerability assessments for this range of distances are negligible.

The seismic shaking caused by the asteroid impact had an absolute magnitude of 2.3 on the Ritcher scale. The absolute magnitude M in (13) is a direct function of the impact energy E. The impact velocity was reduced four orders of magnitude due to the presence of the water layer, which significantly decreased the impact energy and consequentially the seismic shaking magnitude. The absolute magnitude M is the maximum epicentral magnitude value whilst the effective magnitude M_{eff}, obtained with (14), is the magnitude value attenuated by the distance D to the epicentre, in this case the impact site.

The absolute magnitude experienced for the Apophis impact in the deep ocean does not reach alarming values on the Ritcher scale. Thus, as seen in Fig. 7, the effective magnitude M_{eff} as a function of the distance can only decrease, never causing any real threat to any population. Nevertheless, the seismic waves from this hypothetical impact can only reach distances a little over 200 km from the impact site.

The overpressure has a direct relation to the distance D_1 through (16). The yield-scaled distance D_1 in (15) is the distance to a $1Mt$ explosion that experiences the same overpressure effects as the distance

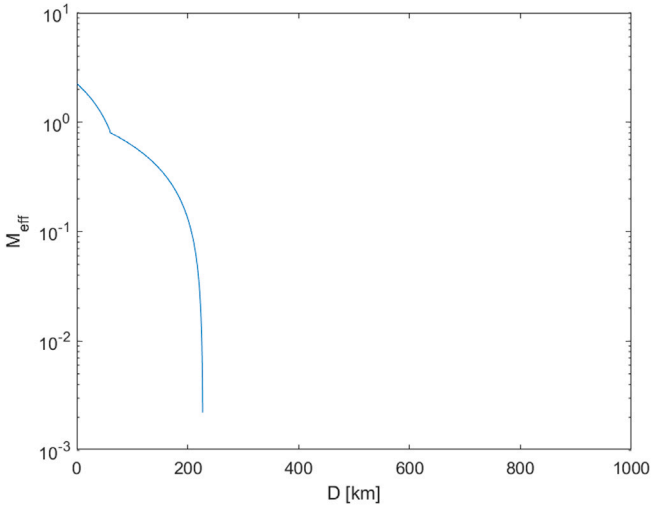

Fig. 7. Effective magnitude as a function of the distance from the Apophis impact location.

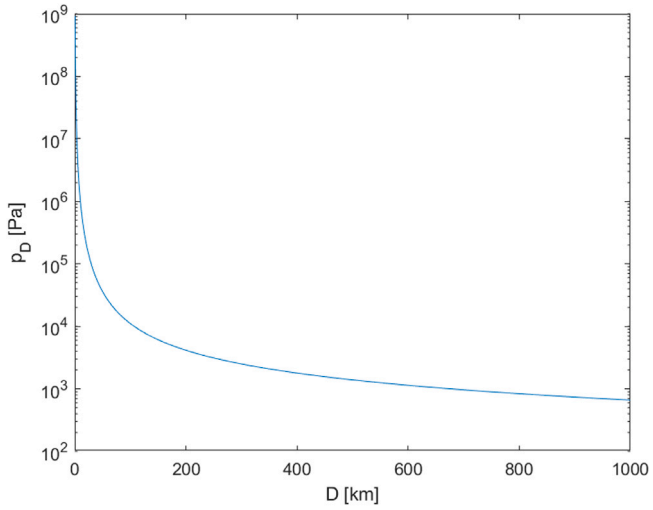

Fig. 8. Overpressure as a function of the distance from the Apophis impact location.

D to the impact energy E. In Fig. 8 the overpressure attenuation with the distance is evident. In the first couple of kilometres, the shock wave intensity felt drops several orders of magnitude. However, even a solid thousand kilometres from the impact are not enough to completely mollify the effects experienced. At this distance, the pressure differential of thousands of Pascals is sufficient to break windows, to cause some destruction to infrastructure and injuries to populations.

The first assessment in the thermal radiation study is the fireball dimension produced at impact. Any other energy transfer method, such as atmospheric heat reflection, was dismissed. The radius of the fireball produced by the Apophis impact, obtained via (17), was $R_f = 3.781 \times 10^3$ m, which falls short of directly influencing any location. This is inferred by assessing the ratio h/R_f, h is the maximum fireball height below the horizon which varies with the distance D, defined in (20), and R_f is naturally the fireball radius. If this ratio is greater than one it means the fireball is entirely below the horizon and the location in question is shielded from direct radiation.

In Fig. 9 we can see the upper ϕ_+ and lower ϕ_- thermal radiation limits defined by the luminous efficiency η_{lum}, both separated by two orders of magnitude. For distances a little over 200 km, both thermal radiation values approach zero, meaning that, due to Earth's curvature, the fireball is entirely below the horizon, and the locations are shielded

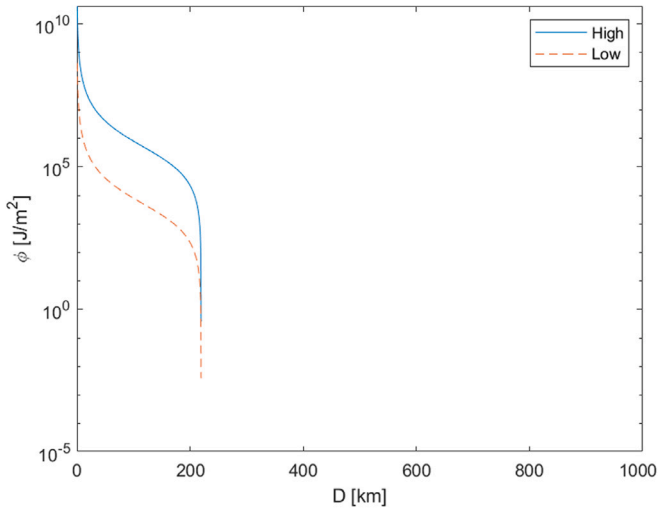

Fig. 9. Thermal radiation as a function of the distance from the Apophis impact location.

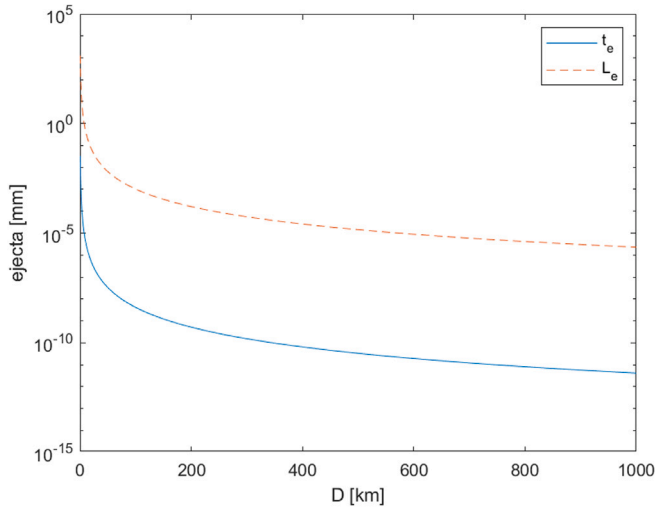

Fig. 10. Ejecta blanket thickness and the mean ejecta fragment diameter as a function of the distance from the Apophis impact location.

from direct exposure. In summation, the thermal radiation experienced near the impact site is significant, but falls off quickly with distance.

Unlike the previous impact effects assessments, the relevant values for the ejected material estimation can be obtained through direct relations. The mean ejecta fragment diameter L_e with (22) and the ejecta blanket thickness t_e with (23). The value used in the vulnerability assessment is the ejecta blanket thickness t_e and to have an impact on population it should be in the centimetre range (Fig. 4), yet in Fig. 10 we can see that this values never reach such magnitudes, staying always below 10^{-4} m. However, the mean fragment diameter L_e, for distances under 100 km lies over the millimetre range, which is a significant ejecta dimension and perceptible to populations. This assessment does not take into consideration that the final crater formation occurs on the bottom of the ocean and the propagation of the ejecta through water. If such was the case, the results would be less significant. Therefore, before the ejecta vulnerability assessment, we can already infer that the ejecta will not play a major role in the deep ocean asteroid impact hazard.

For a deep-water impact, the asteroid generates two distinct type of tsunami waves, rim-waves and collapse waves [28]. As such, the tsunami wave analysis consists of two wave amplitude decay methods.

Table 7
Global implications of the Apophis impact event.

Ratio	Value	Qualitative global change
M_i/M_E	6.4×10^{-15}	No noticeable change in orbit.
Γ_i/Γ_E	8.2×10^{-13}	No noticeable change in rotation period and tilt of axis.
V_{ic}/V_E	4.0×10^{-16}	Earth is not strongly disturbed and loses negligible mass.

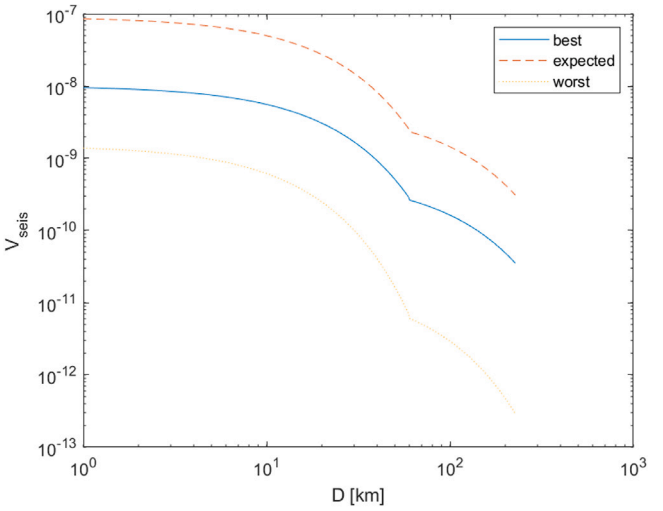

Fig. 11. Effective magnitude vulnerability as a function of the distance from the Apophis impact location.

One rim-wave amplitude method and one collapse wave amplitude decay method. The amplitude models are only valid in deep waters, as such, for the tsunami assessment, the distance the water traverses in deep waters before reaching the shallow water threshold is required. This parameter is obviously highly variant and depends on many factors. To by-pass this location specific variable, a set of three values was chosen to see its influence on the overall tsunami hazard. In shallow waters, the tsunami is evaluated through the run-up assessment, which is wave-invariant, and altitude-dependent. Therefore, the tsunami assessment was made as a function of the distance D from the impact site, the location's altitude h from the sea level, and the shallow water distance D_{shore}.

3.2. Global effects

The impact changes the duration of the day on Earth by about 27 picoseconds, which cannot be perceived by the population. As the asteroid has a relatively small diameter, and impacts Earth with an also relatively small velocity, its qualitative global implications, Table 7, are negligible.

3.3. Vulnerability

The vulnerability assessment is pretty straight forward. Each vulnerability value ranges from zero to one, a zero vulnerability means that the population at the given location is unthreatened by the impact effect, whilst a vulnerability of one means that the entire population is endangered and would perish from the event. In Fig. 11, the seismic shaking vulnerability as a function of the distance can be seen for three different case scenarios, from best to worst. Throughout the plotted domain, the highest value the vulnerability reaches is in the 10^{-7} order, which is a value really close to zero enforcing the innocuous nature of the Apophis-generated seismic waves. As expected, from 227 km outwards, the vulnerability is zero as the corresponding effective magnitude is also zero.

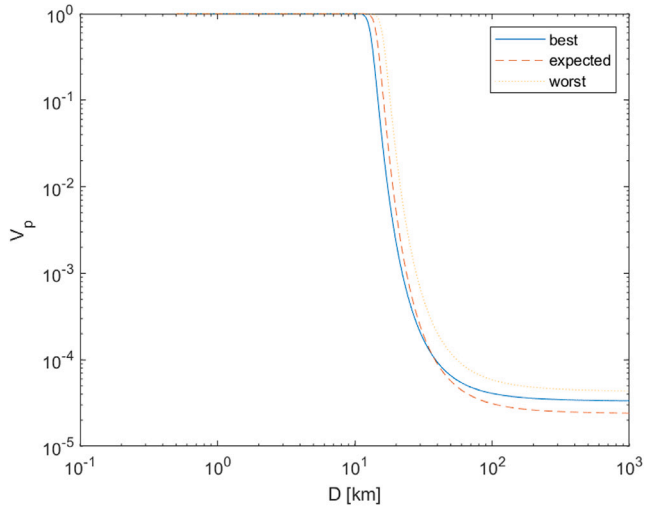

Fig. 12. Overpressure vulnerability as a function of the distance from the Apophis impact location.

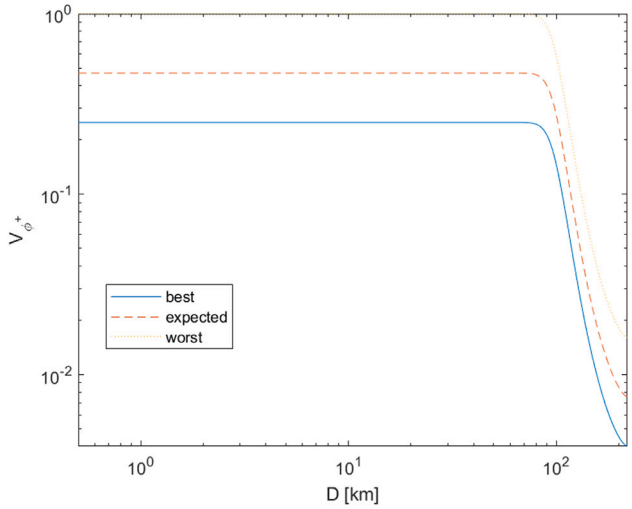

Fig. 14. High thermal radiation vulnerability as a function of the distance from the Apophis impact location.

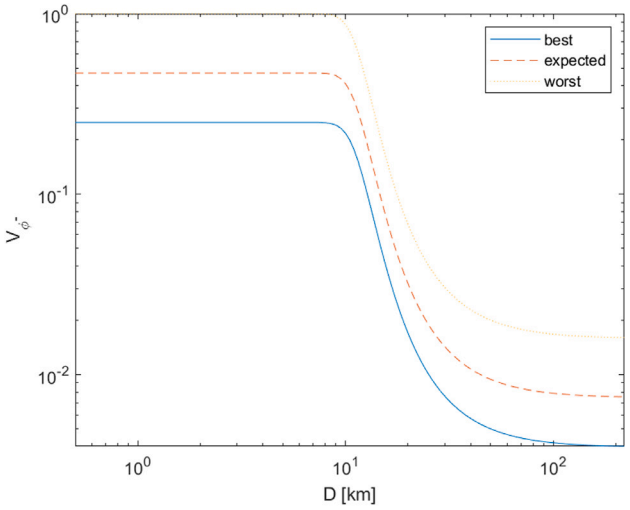

Fig. 13. Low thermal radiation vulnerability as a function of the distance from the Apophis impact location.

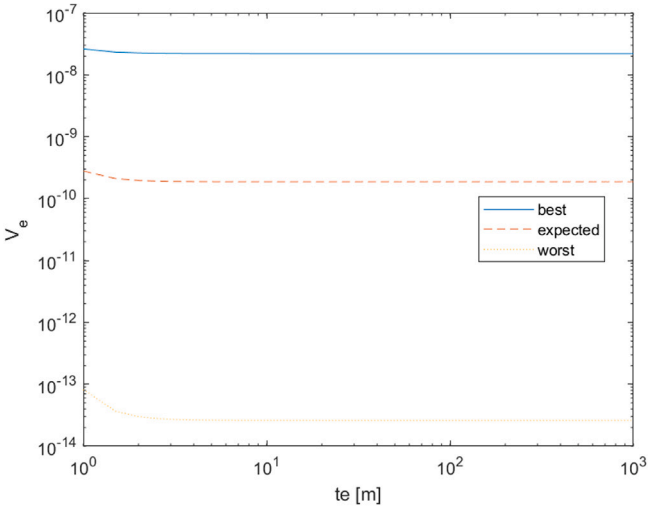

Fig. 15. Ejecta vulnerability as a function of the distance from the Apophis impact location.

In Fig. 12, the pressure vulnerability best-case, expected case, and worst-case scenarios are represented. For distances within a 10 km radius from the impact, the vulnerability is one, *i.e.*, the entire population is exposed. The immense vulnerability decay before the 100 km is also perceptible. This was to be expected as the vulnerability mirrors the pressure differential decay, albeit within a different scale. In the thousand kilometre mark, the vulnerability reaches less alarming values, although this are still relevant since a vulnerability of 10^{-4} on a population of one million results in one hundred casualties. Nevertheless, the best and expected scenarios intersect each other, meaning that from this point onward the terminology loses its meaning and the validity of the vulnerability model can be questioned.

Either the low thermal radiation, Fig. 13, or the high thermal radiation, Fig. 14, entail dangerous vulnerability values in the vicinity on the impact event. Values which, in the worst-case scenario, remain threatening until the 100 km from the impact site. Fortunately for the populations, the thermal radiation decays rapidly with the distance, and from the 220 km outwards, the Earth's curvature completely shields any location from the danger. However, within the affected radial area, the thermal radiation is by far the most concerning Apophis impact effect, as considering the worst-case and the farthermost distances affected, the vulnerability reaches values of 10^{-2}.

Contrasting with the previous vulnerability assessment, the ejecta vulnerability is the least concerning effect. In Fig. 15, the three case scenarios are represented. The values in themselves are low and unconcern, on top of that, the vulnerability model terminology best/worst is swapped, meaning that for such low ejecta values, the vulnerability model validity cannot be credited.

In the tsunami vulnerability analysis, the complexity increased many-fold. To properly assess the vulnerability three location dependent variables are needed, the distance D from the impact, the location's altitude h from the sea level, and the shallow water distance off-coast D_{shore}. Setting three different values for the D_{shore} allowed the simplification of the multi-variable problem and the establishment of the three vulnerability case-scenarios. Therefore the worst-case scenario is defined for $D_{shore} = 1$ km, the expected case when $D_{shore} = 10$ km, and the best-case when $D_{shore} = 100$ km. Throughout Figs. 16–21 the tsunami vulnerability was plotted as a function of the distance and altitude. In every figure, ten gradual-changing colour lines are represented. Each line represents where all the domain has an equal vulnerability, *e.g.* the brightest yellow line represents the locations of

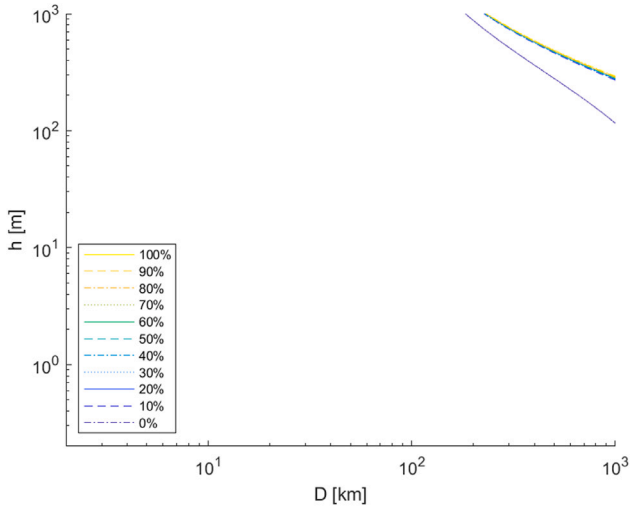

Fig. 16. Rim-wave vulnerability worst-case scenario, when the shallow water distance off the coast D_{shore} is 1 km, as a function of the distance from the Apophis impact location. (For interpretation of the references to colour in this figure legend, the reader is referred to the web version of this article.)

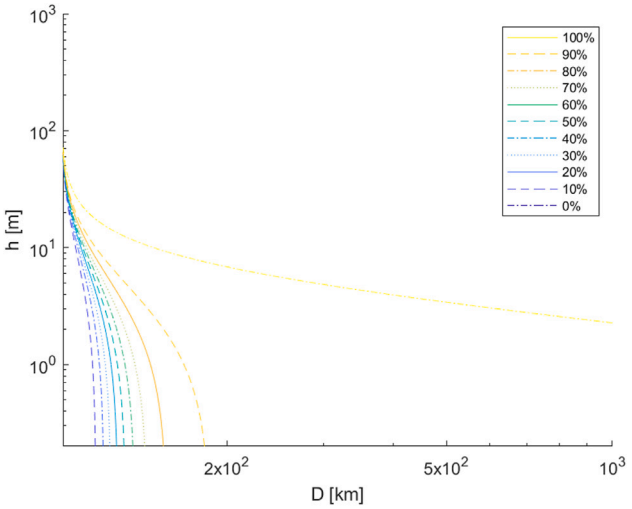

Fig. 18. Rim-wave vulnerability best-case scenario, when the shallow water distance off the coast D_{shore} is 100 km, as a function of the distance from the Apophis impact location. (For interpretation of the references to colour in this figure legend, the reader is referred to the web version of this article.)

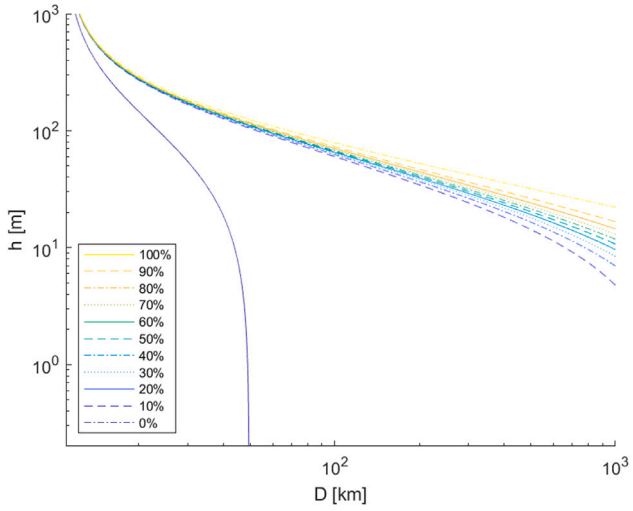

Fig. 17. Rim-wave vulnerability expected case scenario, when the shallow water distance off the coast D_{shore} is 10 km, as a function of the distance from the Apophis impact location. (For interpretation of the references to colour in this figure legend, the reader is referred to the web version of this article.)

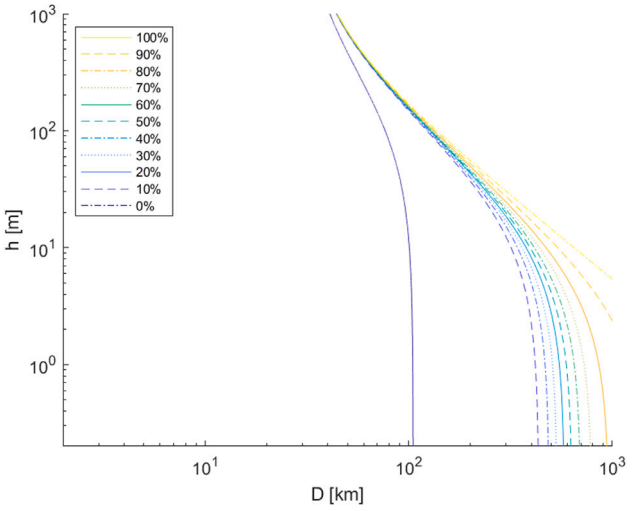

Fig. 19. Collapse wave vulnerability worst-case scenario, when the shallow water distance off the coast D_{shore} is 1 km, as a function of the distance from the Apophis impact location. (For interpretation of the references to colour in this figure legend, the reader is referred to the web version of this article.)

vulnerability one. Naturally, for any line, the side that contains the origin entails vulnerability values greater than the line, and the other side entails values lesser than the line.

In Figs. 16, 17, and 18, the rim-wave vulnerability worst, expected, and best-case scenario are represented respectively. In the worst-case scenario, the domain is almost entirely one for any distance and altitude, making the rim-wave by far the most concerning Apophis impact aftermath. When considering D_{shore} = 10 km, the expected case scenario, the results are less grim. The consequences are still alarming, but there is a large portion of altitude values for which the vulnerability is zero, meaning that the computed run-wave cannot reach such heights. In the best-case scenario, the rim-wave vulnerability is only one for distances a little over 100 km from the impact. In this scenario, most altitudes assessed are safe from the tsunami hazard. For the most part, and independent of the scenario considered, the rim-wave results are worryingly high.

The vulnerability of the final effect assessed, the collapse wave vulnerability is represented in Figs. 19, 20, and 21. Overall, the collapse wave vulnerability mimics the rim-wave vulnerability values. However, the collapse wave model produces smaller vulnerabilities. In the worst-case scenario, locations hundreds of km from the impact and a dozen metres high are completely safe from the incoming wave. In the best-case scenario, most locations would be safe from the collapse wave, but naturally, closer locations would still be endangered.

The asteroid ocean impact results align with the established literature. In [29], the damage contribution per impact effect as casualty numbers and percentage of total casualties of an 200-m asteroid, impacting the water at 20 km/s with a 45° angle, for different offshore distances and water depths are estimated. As the offshore distance and water depth increase, the tendency is for the tsunami casualties to increase and the pressure and thermal radiation to decrease, until the tsunami is isolated and is the only impact effect experienced. Impact effects as seismic shaking and ejecta deposition only account to a minor percentage of the overall casualties. In [30], the effect loss ratio in water impact scenarios per impactor size are obtained. For

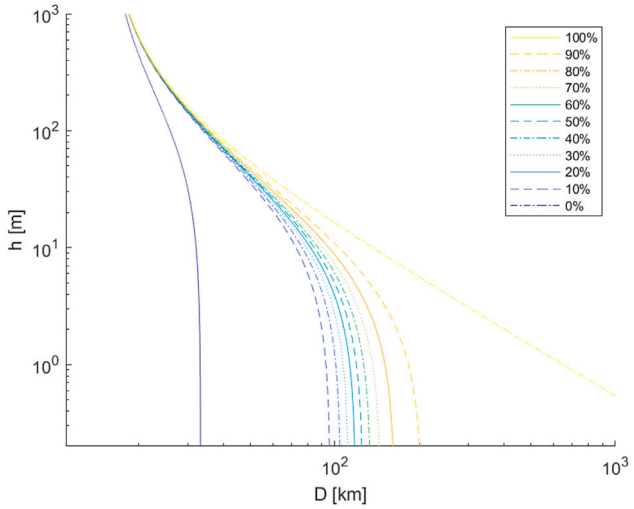

Fig. 20. Collapse wave vulnerability expected case scenario, when the shallow water distance off the coast D_{shore} is 10 km, as a function of the distance from the Apophis impact location. (For interpretation of the references to colour in this figure legend, the reader is referred to the web version of this article.)

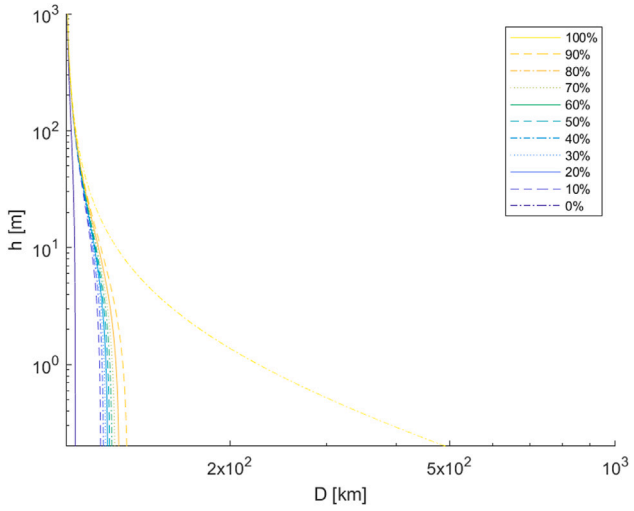

Fig. 21. Collapse wave vulnerability best-case scenario, when the shallow water distance off the coast D_{shore} is 100 km, as a function of the distance from the Apophis impact location. (For interpretation of the references to colour in this figure legend, the reader is referred to the web version of this article.)

a 370-m wide asteroid impact on the water, the tsunami is the most significant impact effects, while effects such as seismic shaking and ejecta deposition provided only minor contributions.

4. Conclusions

The current work studied the short-term effects of an asteroid impact on the ocean. A singular impact was simulated for the Apophis asteroid, a 370-m diameter body. The asteroid was assumed to impact the Earth at a 45° angle with a velocity $v_i = 12.62$ km/s and a density $\rho_i = 3200$ kg/m^3. In addition to the impact effect assessment as a function of the distance and the impact's qualitative global implications, the vulnerabilities were assessed for each impact effect independently.

The impact effects assessment included a seismic shaking event, a shock wave, thermal radiation, ejecta deposit, tsunami waves, and global effects, which includes orbit, rotation period, and tilt of axis changes, as well as mass loss and length of a day variations. The seismic shock can be neglected for the studied ocean impact. The average pressure difference experienced over the distance studied can cause massive structure damage and some potential casualties, however it is not the biggest threat. Thermal radiation is a devastating effect near the impact location but its small reach prevents it from endangering any population more than 220 km away. The infrastructures collapse due to ejecta deposits is the lowest impact threat of an impact on the ocean. The benthic final crater formation plus the distance between the populations and the impact site prevents the deposit of ejected material in populated areas. In deep-water impacts there is a formation of both types of tsunami waves, rim-waves and collapse waves, which are by far the largest threats. To conclude the impact effects assessment, the possible global effects on Earth were considered, and can be disregarded, as there is not a substantial change in any of them.

The vulnerability was assessed through pre-established vulnerability models for all the impact effects studied. All the models are subdivided in three case scenarios: best, expected, and worst.

The impact effect with the highest vulnerability was the rim-wave. In the best-case scenario, it can reach distances a thousand kilometres away and a dozen metres high. In the worst-case scenario, almost all the entire plotted domain has a vulnerability of one. The threat that an asteroid impact-induced tsunami poses to coastal populations around the globe is clear.

Declaration of competing interest

The authors declare that they have no known competing financial interests or personal relationships that could have appeared to influence the work reported in this paper.

Acknowledgements

The present work was performed under the scope of activities at the Aeronautics and Astronautics Research Centre (AEROG) of the Laboratório Associado em Energia, Transportes e Aeronáutica (LAETA), and was supported by the Fundação para a Ciência e Tecnologia by Project No. UIDB/50022/2020; by FCT, through IDMEC, under LAETA, project UIDB/50022/2020; FCT through ICT (Institute of Earth Sciences) project UIDB/04683/2020.

Appendix. Nomenclature

A_{800}	Wave amplitude at the deep/shallow water threshold
A_{cw}	Collapse wave amplitude
A_{cw}^{max}	Collapse wave maximum amplitude
A_{rw}	Rim wave amplitude
A_{rw}^{max}	Rim wave maximum amplitude
C_D	Drag coefficient
D	Distance
D_1	Yield scaled distance
D_c	Threshold diameter between simple and complex craters
D_{fr}	Final crater diameter
D_{shore}	Distance between the municipality and the deep/shallow water threshold point
D_{tc}	Transient crater diameter
D_x	Scaled distance
d_{fr}	Final crater depth
d_{tc}	Transient crater depth

E	Impact energy
E_{kt}	Impact energy in kilotons TNT
f	Ratio of the fireball above the horizon
g_0	Earth standard gravitational acceleration (9.80665 m/s^2)
h	Location altitude
h_f	Fireball maximum height below the horizon
h_{fr}	Rim height
h_{sea}	Sea depth at impact site
L	Asteroid diameter
L_e	Mean ejecta fragment diameter
M	Seismic Ritcher scale magnitude
M_E	Earth linear momentum
M_{eff}	Effective seismic Ritcher scale magnitude
M_i	Impactor linear momentum
m_E	Earth mass
m_i	Impactor mass
R_E	Earth radius
R_f	Fireball radius
p_D	Peak overpressure at distance D
p_e	Load of the ejecta blanket
p_x	Scaled pressure
q	Wave attenuation factor
s	Municipality slope
T_E	Earth rotation period
t_{br}	Breccia lens thickness
t_e	Ejecta blanket thickness
U	Run-up wave height
U_l	Local run-up wave height
V_E	Earth volume
V_{br}	Unbulked Breccia lens volume
V_e	Ejecta blanket deposition vulnerability
V_p	Overpressure vulnerability
V_{seis}	Seismic shaking vulnerability
V_{tc}	Transient crater volume
V_{tsu}	Tsunami vulnerability
V_ϕ	Thermal radiation vulnerability
v_E	Earth mean orbital velocity
v_i	Impact velocity
Γ_E	Earth angular momentum
Γ_i	Impactor angular momentum
Δ	Epicentral angle
ΔT_E	Change in Earth's length of day
η_{lum}	Luminous efficiency
θ	Asteroid impact angle
λ_i	Impact site longitude
λ_k	Municipality longitude
ρ_e	Mean ejecta material density
ρ_i	Impactor density
ρ_t	Target density
ρ_w	Water density
ϕ	Thermal energy per area unit
ϕ_i	Impact site latitude
ϕ_k	Municipality latitude

References

[1] L.W. Alvarez, W. Alvarez, F. Asaro, H.V. Michel, Extraterrestrial cause for the Cretaceous-Tertiary extinction, Science 208 (4448) (1980) 1095–1108, http://dx.doi.org/10.1126/science.208.4448.1095.

[2] K.O. Pope, K.H. Baines, A.C. Ocampo, B.A. Ivanov, Impact winter and the Cretaceous/Tertiary extinctions: Results of a Chicxulub asteroid impact model, Earth Planet. Sci. Lett. 128 (3–4) (1994) 719–725, http://dx.doi.org/10.1016/0012-821x(94)90186-4.

[3] O.P. Popova, P. Jenniskens, V. Emel'yanenko, A. Kartashova, E. Biryukov, S. Khaibrakhmanov, V. Shuvalov, Y. Rybnov, A. Dudorov, V.I. Grokhovsky, et al., Chelyabinsk airburst, damage assessment, meteorite recovery, and characterization, Science 342 (6162) (2013) 1069–1073, http://dx.doi.org/10.1126/science.1242642.

[4] C.R. Chapman, The hazard of near-Earth asteroid impacts on earth, Earth Planet. Sci. Lett. 222 (1) (2004) 1–15, http://dx.doi.org/10.1016/j.epsl.2004.03.004.

[5] T.G. Müller, C. Kiss, P. Scheirich, P. Pravec, L. O'Rourke, E. Vilenius, B. Altieri, Thermal infrared observations of asteroid (99942) Apophis with Herschel, Astron. Astrophys. 566 (2014) A22, http://dx.doi.org/10.1051/0004-6361/201423841.

[6] J. Licandro, T. Müller, C. Alvarez, V. Alí-Lagoa, M. Delbo, GTC/CanariCam observations of (99942) Apophis, Astron. Astrophys. 585 (A10) (2015) http://dx.doi.org/10.1051/0004-6361/201526888.

[7] D. Bancelin, F. Colas, W. Thuillot, D. Hestroffer, M. Assafin, Updated orbit of apophis with recent observations, in: SF2A 2011: Annual Meeting of the French Society of Astronomy and Astrophysics, 2011, pp. 629–634, URL https://hal.sorbonne-universite.fr/hal-00647628.

[8] P. Guo, V.V. Ivashkin, C.A. Stikhno, P.M. Shkapov, Determination and investigation of asteroid Apophis' trajectories set potentially colliding with the Earth in 2036, 468, IOP Publishing, 2018, 012023, http://dx.doi.org/10.1088/1757-899x/468/1/012023,

[9] D. Farnocchia, S.R. Chesley, P.W. Chodas, M. Micheli, D.J. Tholen, A. Milani, G.T. Elliott, F. Bernardi, Yarkovsky-driven impact risk analysis for asteroid (99942) Apophis, Icarus 224 (1) (2013) 192–200, http://dx.doi.org/10.1016/j.icarus.2013.02.020.

[10] D. Vokrouhlický, D. Farnocchia, D. Čapek, S.R. Chesley, P. Pravec, P. Scheirich, T.G. Müller, The yarkovsky effect for 99942 apophis, Icarus 252 (2015) 277–283, http://dx.doi.org/10.1016/j.icarus.2015.01.011.

[11] T. Greicius, NASA Analysis: Earth is safe from asteroid apophis for 100-plus years, 2021, [Online]. Available: https://go.nasa.gov/3roCptG [Accessed: 26-Mar-2021].

[12] A. Morbidelli, W. Jr, P. Michel, Origin and evolution of near-earth objects, 3, 2002, URL https://www.lpi.usra.edu/books/AsteroidsIII/pdf/3003.pdf,

[13] C.R. Chapman, D. Morrison, B. Zellner, Surface properties of asteroids: A synthesis of polarimetry, radiometry, and spectrophotometry, Icarus 25 (1) (1975) 104–130, http://dx.doi.org/10.1016/0019-1035(75)90191-8.

[14] S.J. Bus, R.P. Binzel, Phase II of the small main-belt asteroid spectroscopic survey a feature-based taxonomy, Icarus 158 (1) (2002) 146–177, http://dx.doi.org/10.1006/icar.2002.6856.

[15] R.P. Binzel, A.S. Rivkin, C.A. Thomas, P. Vernazza, T.H. Burbine, F.E. DeMeo, S.J. Bus, A.T. Tokunaga, M. Birlan, Spectral properties and composition of potentially hazardous Asteroid (99942) Apophis, Icarus 200 (2) (2009) 480–485, http://dx.doi.org/10.1016/j.icarus.2008.11.028.

[16] J.C. Reinhardt, M. Daniels, M.E. Paté-cornell, Probabilistic analysis of asteroid impact risk mitigation programs, in: Proceedings of the Probabilistic Safety and Management Conference (PSAM12), 2014, pp. 1–12.

[17] A.F. Cheng, J. Atchison, B. Kantsiper, A.S. Rivkin, A. Stickle, C. Reed, A. Galvez, I. Carnelli, P. Michel, S. Ulamec, Asteroid impact and deflection assessment mission, Acta Astronaut. 115 (2015) 262–269, http://dx.doi.org/10.1016/j.actaastro.2015.05.021.

[18] E.T. Lu, S.G. Love, Gravitational tractor for towing asteroids, Nature 438 (7065) (2005) 177–178, http://dx.doi.org/10.1038/438177a.

[19] B. Wie, Hypervelocity nuclear interceptors for asteroid disruption, Acta Astronaut. 90 (1) (2013) 146–155, http://dx.doi.org/10.1016/j.actaastro.2012.04.028.

[20] C. Bombardelli, H. Urrutxua, M. Merino, J. Pelaez, E. Ahedo, The ion beam shepherd: A new concept for asteroid deflection, Acta Astronaut. 90 (1) (2013) 98–102, http://dx.doi.org/10.1016/j.actaastro.2012.10.019.

[21] C.M. Rumpf, D.L. Mathias, L. Wheeler, J. Dotson, B. Barbee, J. Roa, P. Chodas, D. Farnocchia, Deflection driven evolution of asteroid impact risk under large uncertainties, Acta Astronaut. (2020) http://dx.doi.org/10.1016/j.actaastro.2020.05.026.

[22] G.S. Collins, H.J. Melosh, R.A. Marcus, Earth impact effects program: A web-based computer program for calculating the regional environmental consequences of a meteoroid impact on earth, Meteorit. Planet. Sci. 40 (6) (2005) 817–840, http://dx.doi.org/10.1111/j.1945-5100.2005.tb00157.x.

[23] C.M. Rumpf, Global asteroid risk analysis, 2014, pp. 1–10, http://dx.doi.org/10.13140/2.1.3739.5208, arXiv:1410.4471,

[24] C.M. Rumpf, H.G. Lewis, P.M. Atkinson, Global impact distribution of asteroids and affected population, in: 4th IAA Planetary Defense Conference, 2015, p. 9, URL https://eprints.soton.ac.uk/377825/.

[25] C. Rumpf, H.G. Lewis, P.M. Atkinson, On the influence of impact effect modelling for global asteroid impact risk distribution, Acta Astronaut. 123 (2016) 165–170, http://dx.doi.org/10.1016/j.actaastro.2016.03.015.

[26] C.M. Rumpf, Asteroid Impact Risk (Ph.D. thesis), University of Southampton, 2016, URL https://eprints.soton.ac.uk/412703/.

[27] K. Wünnemann, G.S. Collins, R. Weiss, Impact of a cosmic body into Earth's ocean and the generation of large tsunami waves: Insight from numerical modeling, Rev. Geophys. 48 (4) (2010) http://dx.doi.org/10.1029/2009rg000308.

[28] G.S. Collins, H.J. Melosh, Errata and improvements in earth impact effects program, 2013, URL https://impact.ese.ic.ac.uk/ImpactEarth/ImpactEffects/effects.pdf.

[29] C.M. Rumpf, H.G. Lewis, P.M. Atkinson, Population vulnerability models for asteroid impact risk assessment, Meteorit. Planet. Sci. 52 (6) (2017) 1082–1102, http://dx.doi.org/10.1111/maps.12861.

[30] C.M. Rumpf, H.G. Lewis, P.M. Atkinson, Asteroid impact effects and their immediate hazards for human populations, Geophys. Res. Lett. 44 (8) (2017) 3433–3440, http://dx.doi.org/10.1002/2017GL073191.